

Arbitrary order edge elements for electromagnetic scattering simulations using hybrid meshes and a PML

P. D. Ledger^{*,†}, K. Morgan, O. Hassan and N. P. Weatherill

Department of Civil Engineering, University of Wales Swansea, Swansea SA2 8PP, U.K.

SUMMARY

The use of arbitrary order edge elements for the simulation of two-dimensional electromagnetic scattering problems on hybrid meshes of triangles and quadrilaterals is described. Single-frequency incident waves, generated by a source in the far field, are considered and the solution is determined in the frequency domain. For numerical simulation, the solution domain is truncated at a finite distance from the perfectly conducting scatterer and the non-reflecting boundary condition at the truncated boundary is imposed by the use of a perfectly matched layer (PML). Several examples are included to demonstrate the performance of the proposed procedure. Copyright © 2002 John Wiley & Sons, Ltd.

KEY WORDS: electromagnetic scattering; frequency domain; arbitrary order edge finite elements; hybrid meshes; PML

1. INTRODUCTION

Computational electromagnetics encompasses a wide spectrum of applications and a number of challenging problem areas. A typical example arises in the aerospace industry, where a problem of interest to engineers involved in the development of new designs is the prediction of the radar cross-section of proposed configurations. The computational analysis of this problem requires the simulation of the interaction between electromagnetic waves, generally created by a source located in the far-field, and the complete configuration. Unstructured mesh techniques are attractive for such computations, because fully automatic procedures are available for meshing the complex computational domains that are normally involved. However, standard unstructured mesh solution algorithms employ low-order elements and, for practical problems, where the electrical length of the vehicle can be very large, this results in the requirement for extremely fine meshes [1, 2]. There is, therefore, interest in evaluating the role that could be played in this area by the use of higher order elements, coupled eventually with

*Correspondence to: P. D. Ledger, Department of Civil Engineering, University of Wales Swansea, Swansea SA2 8PP, U.K.

†E-mail: cgledger@swansea.ac.uk

Contract/grant sponsor: Engineering and Physical Sciences Research Council; contract/grant number: GR/M59112

adaptive mesh techniques [3] and, perhaps, fast multipole methods [4]. In addition, hybrid meshes may also have a role to play in reducing the size and complexity of the computational problem. With these points in mind, we describe in this paper an initial study into the frequency-domain simulation of two-dimensional scattering problems. We employ a technique that allows for the use of hybrid triangular and quadrilateral edge elements of arbitrary order and we concentrate attention on the radar cross-section prediction problem.

The $\mathcal{H}(\text{curl}; \Omega)$ conforming finite element approximations for electromagnetics were introduced originally by Nédélec [5–7]. These elements are now known more commonly as edge elements. Since their introduction, edge elements have been the subject of much investigation, with the work of Monk [8, 9], who considered the analysis of various formulations including *hp*-approximations (with p constant), being particularly important. Following this work, Demkowicz and co-workers [10, 11] developed a two-dimensional hierarchical basis for edge elements, which enabled fully adaptive *hp*-approximations to be undertaken on curved domains. The approach adopted here follows these ideas, but employs instead the alternative form for the finite element shape functions defined recently by Ainsworth and Coyle [12]. This form has been shown to possess better conditioning properties and this is particularly important for high-order implementations. Scattering simulations require that a finite computational domain be constructed by truncation of the infinite physical domain at an appropriate distance from the scatterer. For higher order edge elements, Cecot *et al.* [13] addressed the problem of imposing an appropriate condition at the truncated interface by developing a corresponding high-order infinite element. We will employ an alternative approach and describe how a method based upon the addition of an absorbing non-planar artificial perfectly matched layer (PML) [14, 15] can be used to prevent reflection of the outgoing waves from the outer computational boundary that is created by this truncation process.

A number of examples are included to demonstrate the numerical performance of the proposed procedure. The first examples involve scattering by circular cylinders. As exact solutions exist for this geometry, this enables validation of the approach and the development of confidence in the numerical capability. The predictive capability of the method is then illustrated by the inclusion of examples involving scattering by an open cavity and by a NACA0012 aerofoil.

2. PROBLEM STATEMENT

2.1. Governing equations

We are interested in simulating problems in which waves, generated by an electromagnetic source, interact with a perfectly conducting obstacle. It is assumed that the scattering obstacle is surrounded by free space and that the source is located in the far-field. The unknowns are the electric and magnetic field intensity vectors, which are expressed, relative to a cartesian co-ordinate system $Oxyz$, in the form $\mathbf{E} = (E_x, E_y, E_z)^T$ and $\mathbf{H} = (H_x, H_y, H_z)^T$, respectively. For our purposes, it is convenient to decompose these fields into incident and scattered components, according to

$$\mathbf{E} = \mathbf{E}^s + \mathbf{E}^i, \quad \mathbf{H} = \mathbf{H}^s + \mathbf{H}^i \quad (1)$$

where the superscripts i and s denote the incident and scattered fields, respectively. The governing equations for this problem are the Maxwell equations and, if a time variation $e^{i\omega t}$ is assumed, the curl equations may be expressed in the dimensionless form

$$\text{curl } \mathbf{E}^s = -i\omega \boldsymbol{\mu}_f \mathbf{H}^s \quad (2)$$

$$\text{curl } \mathbf{H}^s = i\omega \boldsymbol{\epsilon}_f \mathbf{E}^s \quad (3)$$

and the divergence conditions written as

$$\text{div}(\boldsymbol{\epsilon}_f \mathbf{E}^s) = 0, \quad \text{div}(\boldsymbol{\mu}_f \mathbf{H}^s) = 0 \quad (4)$$

Here $i = \sqrt{-1}$ and $\omega = 2\pi/\lambda$, where λ is the wavelength of the incident wave. Equations (2) and (3) imply that

$$\text{curl}(\boldsymbol{\mu}_f^{-1} \text{curl } \mathbf{E}^s) - \omega^2 \boldsymbol{\epsilon}_f \mathbf{E}^s = \mathbf{0} \quad (5)$$

and

$$\text{curl}(\boldsymbol{\epsilon}_f^{-1} \text{curl } \mathbf{H}^s) - \omega^2 \boldsymbol{\mu}_f \mathbf{H}^s = \mathbf{0} \quad (6)$$

so that both \mathbf{E}^s and \mathbf{H}^s satisfy a reduced vector wave equation. The quantities $\boldsymbol{\mu}_f$ and $\boldsymbol{\epsilon}_f$ represent the relative permeability and relative permittivity, respectively, of the propagation medium. For general media, the entries in these tensors may be complex-valued functions of position, but here, where the medium of propagation is free space, the tensors have the simple form

$$\boldsymbol{\mu}_f = \mathbf{I}, \quad \boldsymbol{\epsilon}_f = \mathbf{I} \quad (7)$$

where \mathbf{I} is the unit tensor.

We further restrict consideration to two-dimensional problems, in which both \mathbf{E}^s and \mathbf{H}^s are functions of x and y only. For transverse electric (TE) simulations, we have $\mathbf{E}^s = (E_x^s, E_y^s, 0)^T$, $\mathbf{H}^s = (0, 0, H_z^s)^T$, and the scattered electric field components will be defined by the solution of Equation (5), with the scattered magnetic field component being obtained, as required, from Equation (2). For transverse magnetic (TM) simulations, we have $\mathbf{E}^s = (0, 0, E_z^s)^T$, $\mathbf{H}^s = (H_x^s, H_y^s, 0)^T$ and, in this case, Equation (6) is solved for the scattered magnetic field components and the scattered electric field component is recovered from Equation (3). It can be shown that the solutions of the reduced vector wave Equations (5) and (6), when combined with the appropriate divergence conditions of Equations (4), are unique [16].

2.2. Boundary conditions

2.2.1. Perfectly conducting scatterer. The scattering obstacle is assumed to be a perfect conductor and the surface of the obstacle forms the internal boundary of the solution domain. On this boundary, the scattered magnetic field is subject to the condition

$$\mathbf{n} \wedge \text{curl } \mathbf{H}^s = -\mathbf{n} \wedge \text{curl } \mathbf{H}^i \quad (8)$$

in TM simulations, where \mathbf{n} represents the unit outward normal vector to the surface and \wedge denotes the vector product. In this case, the surface of the scatterer is denoted by Γ_1 .

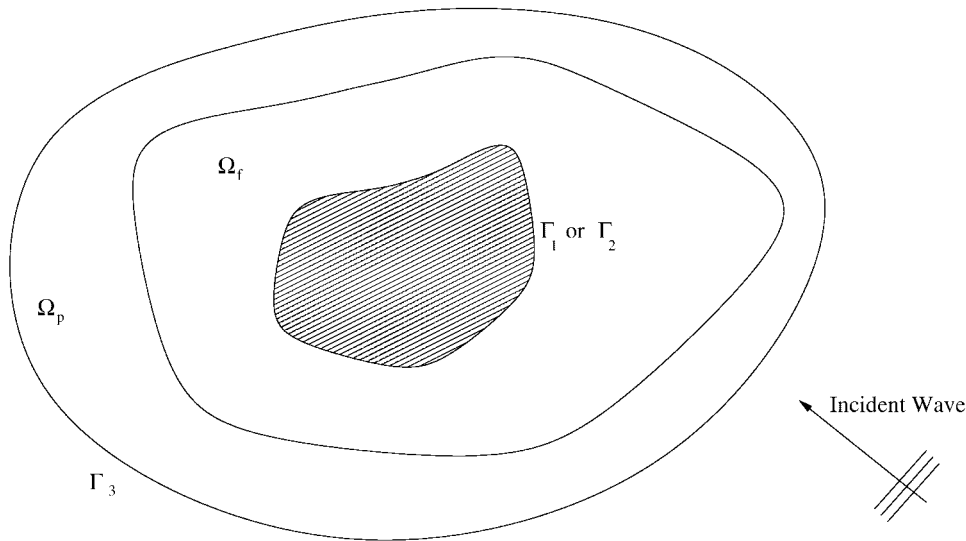


Figure 1. The addition of Ω_p , the PML region, to the domain Ω_f .

In TE simulations, the scattered electric field is subject to the condition

$$\mathbf{n} \wedge \mathbf{E}^s = -\mathbf{n} \wedge \mathbf{E}^i \quad (9)$$

at the surface of the scatterer. In this case, the surface of the scatterer is denoted by Γ_2 .

2.2.2. Far-field treatment. Sufficiently far from the scattering obstacle, the scattered electric and magnetic field components consist of outgoing waves only. Much attention has been devoted to the problem of developing a suitable implementation of this condition, as it is always encountered in the numerical simulation of wave propagation problems defined on infinite domains. The standard approach involves the truncation, at a finite distance, of the infinite domain surrounding the scatterer to create a finite solution domain, Ω_f . At the newly created computational boundary, either absorbing boundary conditions [17, 18], the Dirichlet to Neumann method [19], infinite elements [20, 13] or the wave envelope method [21] may then be employed. Other alternatives involve the coupling of a domain method with a boundary procedure [22] or the use of an iterative method to update the solution on the far-field boundary, using data calculated on the scatterer and an appropriate Green's function [23].

Berenger [14] proposed the alternative PML technique. In his approach, an artificial material layer, Ω_p , is added to the free space domain, Ω_f , at the truncated far-field boundary, as shown in Figure 1. The outer surface of the PML is denoted by Γ_3 . Within the PML, Maxwell's curl equations are considered in the form

$$\text{curl } \mathbf{E}^s = -i\omega\boldsymbol{\mu}_p\mathbf{H}^s \quad (10)$$

$$\text{curl } \mathbf{H}^s = i\omega\boldsymbol{\epsilon}_p\mathbf{E}^s \quad (11)$$

These equations imply that, within the PML,

$$\text{curl}(\boldsymbol{\mu}_p^{-1} \text{curl} \mathbf{E}^s) - \omega^2 \boldsymbol{\varepsilon}_p \mathbf{E}^s = \mathbf{0} \quad (12)$$

and

$$\text{curl}(\boldsymbol{\varepsilon}_p^{-1} \text{curl} \mathbf{H}^s) - \omega^2 \boldsymbol{\mu}_p \mathbf{H}^s = \mathbf{0} \quad (13)$$

We try to choose the thickness of the PML, and to specify the variation in the material properties $\boldsymbol{\varepsilon}_p$ and $\boldsymbol{\mu}_p$ through the PML, so as to ensure that the scattered wave is completely absorbed within the layer, without reflection. At the outer surface, Γ_3 , the boundary condition

$$\mathbf{n} \wedge \mathbf{E}^s = \mathbf{0} \quad (14)$$

is applied in TE simulations, while the condition

$$\mathbf{n} \wedge \mathbf{H}^s = \mathbf{0} \quad (15)$$

is applied in the TM case.

2.3. Variational formulation

The governing differential equations (5), (6), (12) and (13) for this problem may be combined and written in the form

$$\text{curl}(\boldsymbol{\Lambda}_1^{-1} \text{curl} \mathbf{U}^s) - \omega^2 \boldsymbol{\Lambda}_2 \mathbf{U}^s = \mathbf{0} \quad (16)$$

where the unknown vector \mathbf{U}^s is to be interpreted as the scattered electric field for the TE case and the scattered magnetic field in TM simulations. In addition, within Ω_f we take

$$\boldsymbol{\Lambda}_1 = \boldsymbol{\Lambda}_2 = \mathbf{I} \quad (17)$$

while in Ω_p

$$\boldsymbol{\Lambda}_1 = \boldsymbol{\mu}_p, \quad \boldsymbol{\Lambda}_2 = \boldsymbol{\varepsilon}_p \quad (18)$$

for TE simulations and

$$\boldsymbol{\Lambda}_1 = \boldsymbol{\varepsilon}_p, \quad \boldsymbol{\Lambda}_2 = \boldsymbol{\mu}_p \quad (19)$$

in the TM case. To develop a numerical solution procedure, a variational formulation of this problem is employed. Defining the spaces Z and Z^D as

$$Z = \{\mathbf{v} \mid \mathbf{v} \in \mathcal{H}(\text{curl}; \Omega); \mathbf{n} \wedge \mathbf{v} = -\mathbf{n} \wedge \mathbf{U}^i \text{ on } \Gamma_2; \mathbf{n} \wedge \mathbf{v} = \mathbf{0} \text{ on } \Gamma_3\} \quad (20)$$

$$Z^D = \{\mathbf{v} \mid \mathbf{v} \in \mathcal{H}(\text{curl}; \Omega); \mathbf{n} \wedge \mathbf{v} = \mathbf{0} \text{ on } \Gamma_2, \mathbf{n} \wedge \mathbf{v} = \mathbf{0} \text{ on } \Gamma_3\} \quad (21)$$

then a weak variational formulation of the problem is: find $\mathbf{U}^s \in Z$, such that

$$\int_{\Omega_f + \Omega_p} (\boldsymbol{\Lambda}_1^{-1} \text{curl} \mathbf{U}^s \cdot \text{curl} \mathbf{v} - \omega^2 \boldsymbol{\Lambda}_2 \mathbf{U}^s \cdot \mathbf{v}) d\Omega + \int_{\Gamma_1} (\mathbf{n} \wedge \boldsymbol{\Lambda}_1^{-1} \text{curl} \mathbf{U}^s) \cdot \mathbf{v} d\Gamma = 0 \quad (22)$$

for all \mathbf{v} in Z^D . It should be noted that, to be mathematically precise, the enforcement of the divergence conditions of Equation (4) requires the use of a Lagrange multiplier [10]. In this

case, \mathbf{U}^s is replaced by $\mathbf{U}^s + \text{grad } p$, with $p \in \mathcal{H}^1(\Omega)$. However, for the scattering problems which are of interest here, which involve prescribed non-zero values for ω , the formulation employed will ensure that the Lagrange multiplier, p , is identically equal to zero [11].

3. NUMERICAL ALGORITHM

3.1. Finite element discretization

The computational domain $\Omega_f + \Omega_p$ is sub-divided into a general assembly of triangular and quadrilateral edge elements. Triangular elements are used in the region that is bounded internally by the scatterer and externally by a circle of prescribed radius. The outer boundary, Γ_3 , is taken to be a circle and the remainder of the computational domain is then divided into a structured mesh of quadrilaterals. A numerical solution of the problem is obtained by employing the Galerkin method of approximation to the variational formulation of Equation (22). In computational electromagnetics, extensive use has been made of the Whitney element [24], which is the lowest order triangular edge element. Edge elements are constructed to give an approximation of the $\mathcal{H}(\text{curl}; \Omega)$ space in which the tangential component of the solution is continuous across element edges. For the Whitney element, the tangential component of the solution is constant along each edge. The level of accuracy achieved by this element is therefore low and fine meshes must be used for the solution of practical problems. Consequently, researchers have begun to explore the use of higher order edge elements, where the field is approximated to a higher degree. In this context, Webb and Forghani [25] presented a hierarchical scheme for triangular elements up to order 4, in which the lowest order element was the Whitney element. Similar developments for quadrilateral edge elements have generally tended to have been undertaken separately, so that, although higher order quadrilateral elements exist [26], they are not always directly compatible with the triangular elements.

This compatibility problem was first successfully addressed by Demkowicz and Rachowicz [10], who developed a scheme of compatible, arbitrary order, quadrilateral and triangular edge elements. Recently, Ainsworth and Coyle [12] have developed a new family of compatible arbitrary order quadrilateral and triangular elements, with better conditioning properties, and these elements are adopted here.

3.1.1. Quadrilateral element basis functions. The master quadrilateral element is taken to be the square $-1 \leq \xi, \eta \leq 1$. For an element of order p , the variation of the unknown field over this element is approximated as

$$\mathbf{U}^s(\xi, \eta) = \sum_{i=1}^4 \sum_{j=0}^p e_j^i \phi_j^i + \sum_{j=0}^p \sum_{k=1}^p e_{j,k}^{I_\xi} \phi_{j,k}^{I_\xi} + \sum_{j=0}^p \sum_{k=1}^p e_{j,k}^{I_\eta} \phi_{j,k}^{I_\eta} \quad (23)$$

In this expression, ϕ denotes the vector form of the shape functions, while the scalars e are the unknowns. The basis functions ϕ_j^i of order j ; $j = 0, 1, \dots, p$, are associated with the element edges i ; $i = 1, 2, 3, 4$. These functions involve Legendre polynomials. For an efficient numerical implementation, we use a recursive relation [27] to generate the higher order terms. The basis functions $\phi_{j,k}^{I_\xi}$ and $\phi_{j,k}^{I_\eta}$ are associated with the interior of the element and have vanishing tangential component on the element edges. These functions involve the integrated

Legendre polynomials which are again computed using a recursive relation [27]. We note that the interior basis functions are only included when $p \geq 1$.

3.1.2. Triangular element basis functions. The master triangular edge element is taken to be the equilateral triangle with vertices $(1, 0)$, $(0, \sqrt{3})$ and $(-1, 0)$. Over this element, the variation of the unknown field is represented to order p , as

$$\mathbf{U}^s(\xi, \eta) = \sum_{i=1}^3 \sum_{j=0}^p e_j^i \phi_j^i + \sum_{i=1}^3 \sum_{j=0}^{p-2} e_{i,j}^{\text{PI}} \phi_{i,j}^{\text{PI}} + \underbrace{\sum_{j=0}^{p-3} \sum_{k=0}^{p-3} e_{j,k}^{\text{GI}_\xi} \phi_{j,k}^{\text{GI}_\xi}}_{j+k \leq p-3} + \underbrace{\sum_{j=0}^{p-3} \sum_{k=0}^{p-3} e_{j,k}^{\text{GI}_\eta} \phi_{j,k}^{\text{GI}_\eta}}_{j+k \leq p-3} \quad (24)$$

The basis functions ϕ_j^i of order j ; $j = 0, 1, \dots, p$, are now associated with the element edges i ; $i = 1, 2, 3$. The pseudo-interior basis functions $\phi_{i,j}^{\text{PI}}$ where $j = 0, 1, \dots, p-2$, are added for $p \geq 2$. These functions are such that their tangential component vanishes on the triangle edges. Finally, the genuine interior basis functions $\phi_{j,k}^{\text{GI}_\xi}$ and $\phi_{j,k}^{\text{GI}_\eta}$ are also included for $p \geq 3$. These functions involve the Jacobi polynomials which are generated numerically by using a recursive relation [27]. We note that the genuine interior functions vanish on all the element edges.

3.2. Specification of the PML

The PML, Ω_p , is always taken to be in the form of a circular annulus of thickness 0.75λ and lies within the region that has been discretized with a structured mesh of quadrilaterals. In the PML, the entries in Λ_1 and Λ_2 are defined [15] to be complex-valued functions of position, according to

$$\Lambda_1 = \Lambda_2 = \Lambda = \begin{bmatrix} \Lambda'' & 0 \\ 0 & \alpha \end{bmatrix} \quad (25)$$

where

$$\Lambda'' = \mathbf{J}^T \begin{bmatrix} \alpha & 0 \\ 0 & \alpha^{-1} \end{bmatrix} \mathbf{J}, \quad \alpha = 1 - (i\sigma/\omega) \quad (26)$$

and \mathbf{J} is a rotation matrix. The PML parameter, σ , is defined to vary quadratically through the layer, as

$$\sigma(x, y) = \sigma_{\max}(r - r_1)^2 / 0.5625\lambda^2 \quad (27)$$

where r denotes the radial distance from the centre of the annulus to the point (x, y) and r_1 is the radius of the inner circle of the annulus. The optimum value

$$\sigma_{\max} = 11/\lambda \quad (28)$$

has been determined as a result of a series of numerical experiments and is employed in all the computations reported in this paper.

3.3. Construction and solution of the linear equation system

The application of the Galerkin approximation to the variational formulation of Equation (22) results in the formation of a complex linear equation system. This system may be expressed in the matrix form

$$\mathbf{K}\mathbf{e} = \mathbf{r} \quad (29)$$

where typical entries in the coefficient matrix, \mathbf{K} , and the right-hand side vector, \mathbf{r} , are given by

$$K_{\beta\gamma} = \int_{\Omega_f + \Omega_p} (\Lambda_1^{-1} \text{curl } \mathbf{v}_\gamma \cdot \text{curl } \mathbf{v}_\beta - \omega^2 \Lambda_2 \mathbf{v}_\gamma \cdot \mathbf{v}_\beta) \, dx \, dy \quad (30)$$

and

$$r_\beta = \int_{\Gamma_2} (\mathbf{n} \wedge \Lambda_1^{-1} \text{curl } \mathbf{U}^i) \cdot \mathbf{v}_\beta \, d\Gamma \quad (31)$$

where \mathbf{v}_β denotes a typical basis function. These integrals are evaluated by employing covariant projections [28] to map, in turn, each element in the problem domain $\Omega_p + \Omega_f$ into the master element. For the purposes of this paper, this is accomplished by using either a standard bilinear or a linear mapping function. For quadrilateral elements, with vertices located at $(x_i, y_i); i = 1, 2, 3, 4$, the bilinear mapping

$$\begin{bmatrix} x \\ y \end{bmatrix} = \sum_{i=1}^4 \begin{bmatrix} x_i \\ y_i \end{bmatrix} N_i(\xi, \eta) \quad (32)$$

is used where $N_i(\xi, \eta)$ is the conventional bilinear finite element shape functions associated with vertex i of the master element. For triangular elements, with vertices located at $(x_i, y_i); i = 1, 2, 3$, the linear mapping

$$\begin{bmatrix} x \\ y \end{bmatrix} = \sum_{i=1}^3 \begin{bmatrix} x_i \\ y_i \end{bmatrix} \vartheta_i(\xi, \eta) \quad (33)$$

is adopted, where $\vartheta_1, \vartheta_2, \vartheta_3$ are the area co-ordinates of the master triangle. It is accepted that this mapping may require refinement of the mesh in the vicinity of the scatterer to ensure that the boundary shape is adequately resolved. However, it should be noted that accurate boundary resolution can be achieved, at additional computational complexity, if the mapping is constructed with blending functions [29].

Using the mapping, the typical entry, $K_{\beta\gamma}$, in the left-hand side matrix defined in Equation (30), may be evaluated by assembling the element contributions

$$K_{\beta\gamma}^e = \int \int [(\Lambda_1^{-1} \text{curl } \mathbf{v}_\gamma \cdot \text{curl } \mathbf{v}_\beta - \omega^2 \Lambda_2 \mathbf{v}_\gamma \cdot \mathbf{v}_\beta) | \mathbf{a}_\xi \cdot \mathbf{a}_\eta \wedge \mathbf{a}_z |]_e \, d\xi \, d\eta \quad (34)$$

where e denotes a typical element in the mesh and the integration is performed over the mapped master element. Defining the contravariant vectors

$$\mathbf{a}^\xi = \frac{\mathbf{a}_\eta \wedge \mathbf{a}_z}{\mathbf{a}_\xi \cdot \mathbf{a}_\eta \wedge \mathbf{a}_z}, \quad \mathbf{a}^\eta = \frac{\mathbf{a}_z \wedge \mathbf{a}_\xi}{\mathbf{a}_\xi \cdot \mathbf{a}_\eta \wedge \mathbf{a}_z} \quad (35)$$

where

$$\mathbf{a}_\xi = \left[\frac{\partial x}{\partial \xi}, \frac{\partial y}{\partial \xi}, 0 \right]^T, \quad \mathbf{a}_\eta = \left[\frac{\partial x}{\partial \eta}, \frac{\partial y}{\partial \eta}, 0 \right]^T, \quad \mathbf{a}_z = [0, 0, 1]^T \quad (36)$$

the basis function \mathbf{v}_β on element e may be evaluated as [28]

$$[\mathbf{v}_\beta(x, y)]_e = [v_{\beta\xi}\mathbf{a}_\xi + v_{\beta\eta}\mathbf{a}_\eta]_e \quad (37)$$

Here, $v_{\beta\xi}$ and $v_{\beta\eta}$ denote covariant components on the mapped master element. In addition, the expression

$$[\text{curl } \mathbf{v}_\beta(x, y)]_e = \frac{1}{|\mathbf{a}_\xi \cdot \mathbf{a}_\eta \wedge \mathbf{a}_z|_e} \begin{bmatrix} 0 \\ 0 \\ \frac{\partial v_{\beta\eta}}{\partial \xi} - \frac{\partial v_{\beta\xi}}{\partial \eta} \end{bmatrix}_e \quad (38)$$

is employed [28] to determine the variation of $\text{curl } \mathbf{v}_\beta$ over element e .

On assembling the element contributions, it is beneficial to employ static condensation [30] to achieve an initial elimination of the interior degrees of freedom for higher order elements. Additional computational efficiency is achieved by optimization of the edge numbering to minimize the bandwidth of the linear equation system. This is accomplished by using a standard Cuthill–McKee algorithm [31]. The resulting equation system is solved using a direct LINPACK solver.

3.4. Computation of the scattering width

For two-dimensional TE problems, the radar cross-section per unit length, or the scattering width, is defined as

$$\chi = \lim_{r \rightarrow \infty} 2\pi r \frac{|H_z^s|^2}{|H_z^i|^2} \quad (39)$$

Using a near-field to far-field transformation [32], the scattering width can be evaluated as

$$\chi = \frac{\omega}{4} \left| \int_{\Gamma_2} (W_2 \cos \phi - W_1 \sin \phi + W_3) e^{i\omega(x' \cos \phi + y' \sin \phi)} d\Gamma \right|^2 \quad (40)$$

where (x', y') denotes the co-ordinates of a general point on the scatterer and

$$\mathbf{W} = \begin{bmatrix} W_1 \\ W_2 \\ W_3 \end{bmatrix} = \begin{bmatrix} n_y H_z^s \\ -n_x H_z^s \\ n_y E_x^s - n_x E_y^s \end{bmatrix} \quad (41)$$

In these equations, r and ϕ denote the cylindrical polar co-ordinates of a general observation point in the far-field and n_x and n_y are the components of the outward normal vector on the scatterer. Similar expressions can be employed for the TM case. When the results of the

numerical simulations are presented, it is the quantity

$$\text{RCS} = 10 \log_{10} \chi \quad (42)$$

that will be plotted.

4. NUMERICAL EXAMPLES

4.1. Scattering by circular cylinders

Exact analytical solutions exist for problems involving perfectly conducting circular cylindrical scatterers [33] and such problems are ideal for the purpose of validating the numerical procedure. The axis of the cylinder is assumed to lie along the z -axis. For a TE simulation, the exact distribution of the scattering width is given by

$$\chi = \frac{4}{\omega} \left| \sum_{n=-\infty}^{\infty} \frac{J'_n(\omega a)}{H_n^{(2)'}(\omega a)} e^{in\phi} \right|^2 \quad (43)$$

where J_n is the Bessel function of the first kind, $H_n^{(2)}$ is the Hankel function of the second kind and a is the radius of the cylinder. The corresponding expression

$$\chi = \frac{4}{\omega} \left| \sum_{n=-\infty}^{\infty} \frac{J_n(\omega a)}{H_n^{(2)}(\omega a)} e^{in\phi} \right|^2 \quad (44)$$

describes the exact distribution of the scattering width for a TM simulation.

4.1.1. Cylinder of electrical length 2λ . The first example involves the scattering of a plane TE wave by a perfectly conducting circular cylinder. The electrical length of the cylinder is 2λ , so that $2\lambda = 2a$. The value $a = 1$ is employed. For this case, a structured hybrid mesh consisting of two layers of triangles and six layers of quadrilaterals is generated so that the far-field boundary, Γ_3 , is the circle of radius 2λ . The PML is taken to coincide with the region of quadrilateral elements as this region is of thickness 0.75λ . An illustration of this hybrid mesh is shown in Figure 2. The RCS distributions computed on this mesh, using elements of uniform order $p = 0, 1, 2, 3, 4, 5$ in turn, are displayed in Figure 3. It can be observed that the distribution obtained using $p = 0$ is asymmetric. However, the distribution becomes symmetric, and mesh convergence is achieved, as the polynomial order is increased. The results of the corresponding TM simulation, using the same mesh, are shown in Figure 4.

To illustrate the performance of the method employed for the treatment of the far-field boundary, the results obtained with the PML are compared with those produced by using a standard second-order Bayliss–Turkel absorbing boundary condition [34]. An edge element implementation of this boundary condition has been described previously [24]. Figure 5 compares the exact and the computed RCS distributions for the TE simulation. When edge elements of order $p = 4$ are employed throughout the mesh, the results produced with both the Bayliss–Turkel and the PML boundary conditions are seen to be in excellent agreement with the exact distribution of Equation (43). The comparison of the computed distributions of the RCS for the corresponding TM simulation is shown in Figure 6. Again edge elements of constant

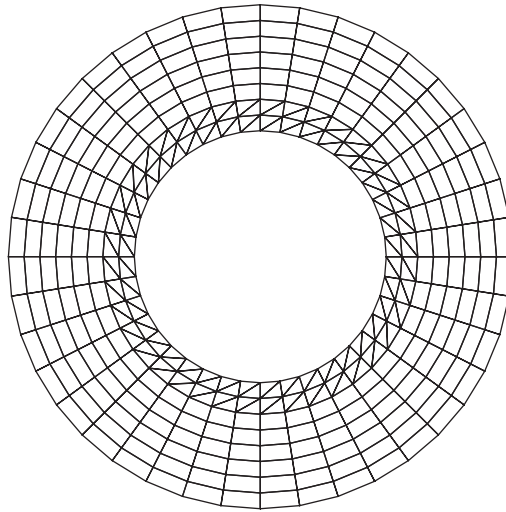


Figure 2. A structured hybrid mesh consisting of 160 triangles and 240 quadrilaterals.

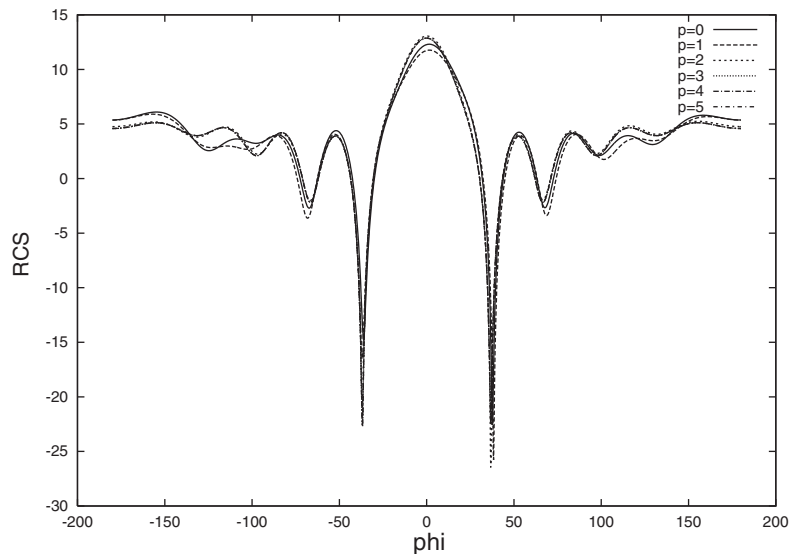


Figure 3. Scattering of a TE wave by a circular cylinder of electrical length 2λ : convergence of the RCS distribution with increase in p .

order $p=4$ are employed throughout the mesh. However, in this case, it is clear that the prediction produced when the PML is employed is superior to that obtained by the use of the absorbing boundary condition. The PML distribution is in near perfect agreement with the exact solution of Equation (44), while the distribution produced with the absorbing boundary condition exhibits large oscillations. Further increase in the polynomial order does not reduce these oscillations and it is only when the boundary Γ_3 is moved out to a radius of 5λ that

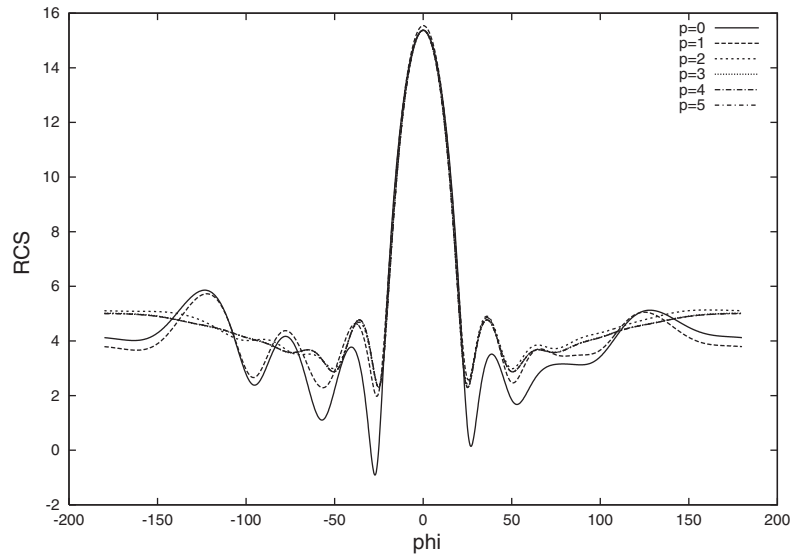


Figure 4. Scattering of a TM wave by a circular cylinder of electrical length 2λ : convergence of the RCS distribution with increase in p .

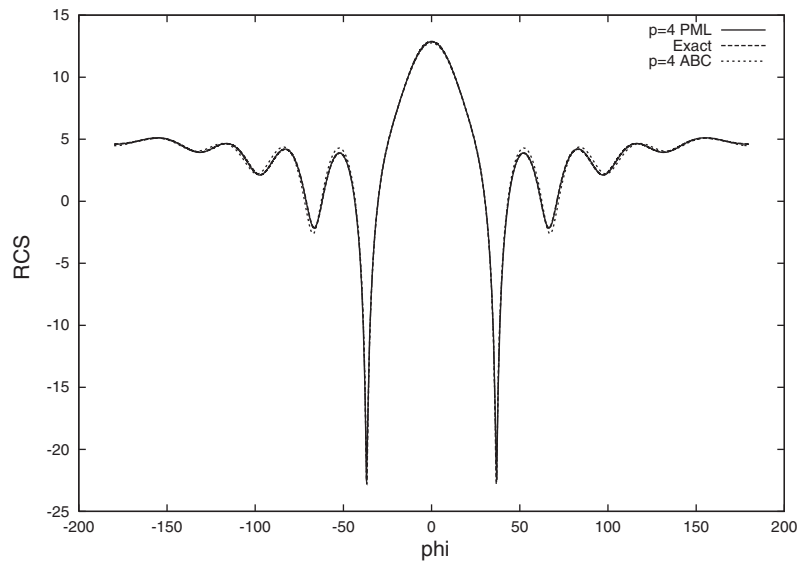


Figure 5. Scattering of a TE wave by a circular cylinder of electrical length 2λ : comparison between the exact distribution and the results computed using both a PML and an absorbing boundary condition.

these oscillations are dampened. This illustrates the effectiveness of the PML treatment of the far-field boundary condition, as the requirement for increasing the problem domain size is accompanied by a corresponding increase in the number of unknowns and a three-fold increase in the computer time.

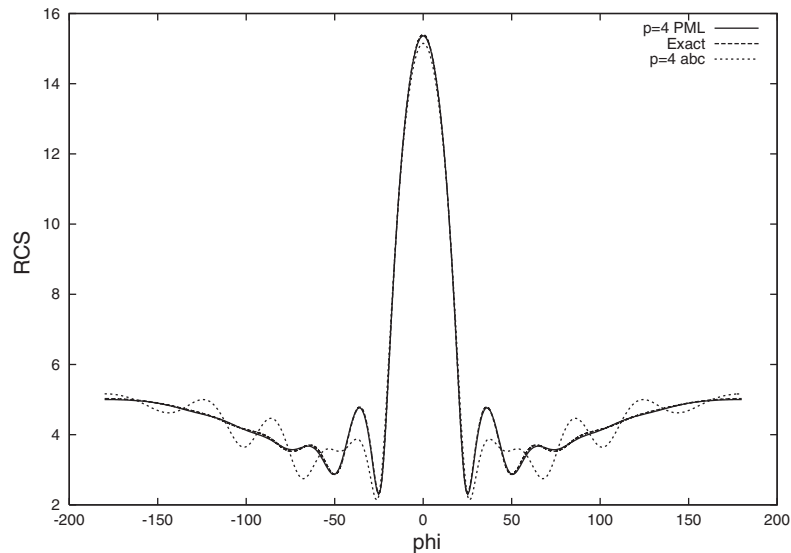


Figure 6. Scattering of a TM wave by a circular cylinder of electrical length 2λ : comparison between the exact distribution and the results computed using both a PML and an absorbing boundary condition.

4.1.2. Cylinder of electrical length 15λ . The next example involves the computationally more challenging problem of scattering by a perfectly conducting circular cylinder of electrical length 15λ i.e. the diameter of the cylinder $2a = 15\lambda$. Again the value $a = 1$ is adopted. As λ decreases, relative to the size of the scatterer, the accurate resolution of the geometry of the scatterer becomes more important [35] and, for this reason, we increase the number of elements in the radial direction in the structured mesh. This results in a mesh consisting of 600 quadrilaterals and 400 triangles, as illustrated in Figure 7. The outer surface of this mesh is again the circle of radius 2. However, the PML layer for this example occupies only the final layer of quadrilaterals before the outer boundary Γ_3 .

The order of approximation employed is increased uniformly across the mesh until convergence of the RCS distribution is obtained. Following this approach, convergence of the solution is obtained for $p = 6$. The converged RCS distribution is seen to be in excellent agreement with the exact distribution in Figure 8. The corresponding comparison for the TM simulation is shown in Figure 9 and again the agreement is good. The small oscillations which appear in the TM case at large viewing angles are caused by reflections from the PML layer. Recent work has shown that these oscillations can be removed by replacing the far-field condition $\mathbf{n} \wedge \mathbf{U}^s = \mathbf{0}$ on Γ_3 with a simple absorbing boundary condition [29].

4.2. Scattering by obstacles of more general shape

To illustrate the predictive capability of the procedure, we now consider the simulation of problems involving scatterers of more complex shape, for which no analytical solution is available. The simulations included involve scattering by a semi-open cavity and by a NACA0012 aerofoil. For these non-cylindrical scatterers, an advancing front procedure [36] is employed

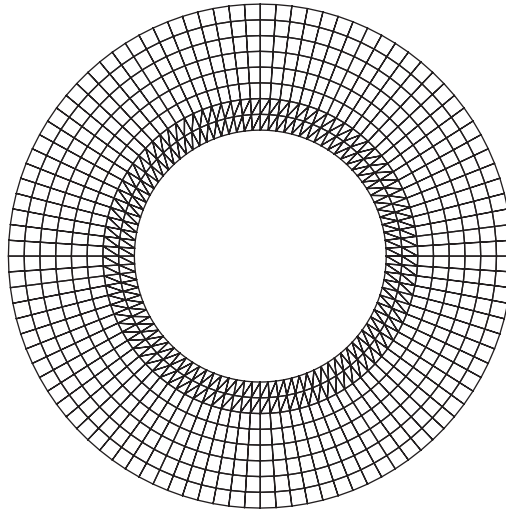


Figure 7. A structured hybrid mesh consisting of 400 triangles and 600 quadrilaterals.

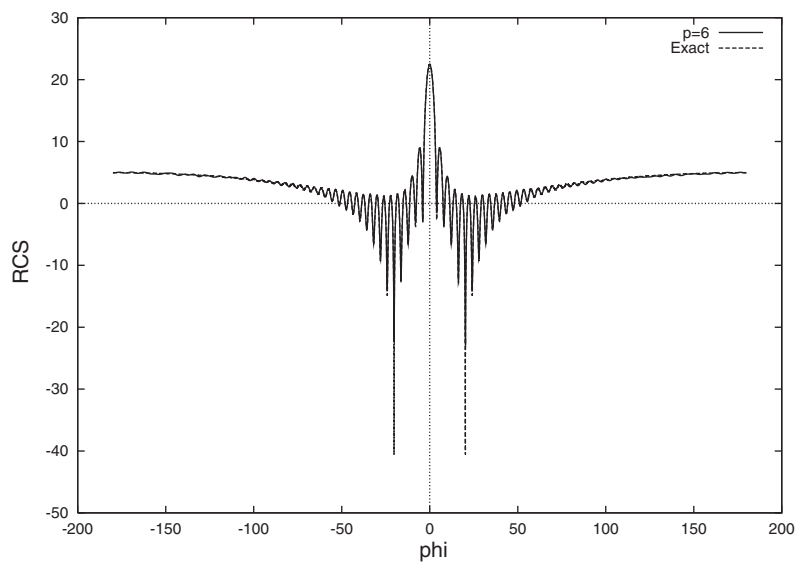


Figure 8. Scattering of a TE wave by a circular cylinder of electrical length 15λ : comparison between the exact and computed RCS distributions.

initially to generate a truly unstructured mesh of triangles. A structured mesh of quadrilaterals is then attached to the outer surface of the triangulated region and is terminated at the desired distance from the scatterer. The PML lies within this structured mesh region. The location of the interface between the quadrilateral and triangular elements can be arbitrarily located and the number of layers of elements in the structured mesh may be arbitrarily defined. However,

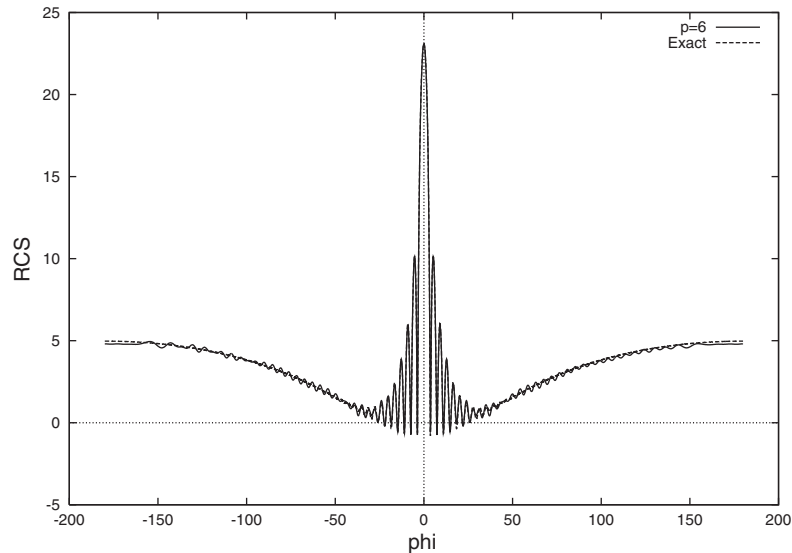


Figure 9. Scattering of a TM wave by a circular cylinder of electrical length 15λ : comparison between the exact and computed RCS distributions.

in practice, we attempt to ensure that the hybrid meshes which are a result of approximately uniform spacing.

4.2.1. Semi-open cavity. Geometrically, the perfectly conducting semi-open cavity consists of two parallel walls which are connected at their right-hand end. This produces a cavity in the shape of a letter U rotated through 90° . The thickness of the walls is denoted by t and the outer dimensions are given by $b + t$ in the x direction and $c + 2t$ in the y direction. The implication here is that the inner cavity has dimensions b and c . We consider the particular cavity which is defined by the specific values $t = 0.4\lambda = 0.2$, $b = 8\lambda = 4$ and $c = 2\lambda = 1$. A TE simulation is performed in which the incident wave propagates in a direction which lies at an angle of $\theta = 30^\circ$ to the x -axis. An unstructured mesh of triangles is generated within the region bounded by a circle of radius 3 and a structured mesh, consisting of one layer of quadrilaterals of thickness 0.75 in this case, is then attached. A view of this mesh is given in Figure 10. The PML layer for this example occupies only the last half of the structured layer of quadrilaterals.

The order of approximation employed is increased uniformly across the mesh until convergence of the RCS distribution is obtained. Following this approach, convergence of the solution is obtained for $p = 8$. The corresponding contours of the real and imaginary components of the scattered magnetic field are shown in Figures 11 (a) and 11(b). The converged distribution of the RCS is compared in Figure 12 with the distribution produced by a finite element time-domain solution approach [37]. The two RCS distributions are very similar, although at some locations the time-domain solution does not reproduce the sharp troughs that are apparent in the frequency-domain solution. These differences may be attributed to the low accuracy of the far-field boundary condition in the time-domain computational procedure.

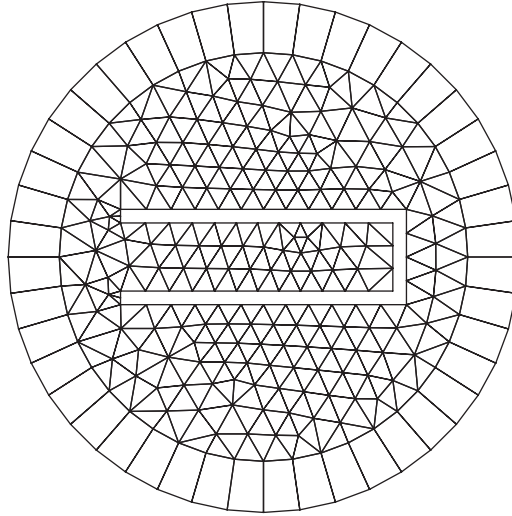


Figure 10. A hybrid mesh for the semi-open cavity consisting of 407 triangles and 44 quadrilaterals.

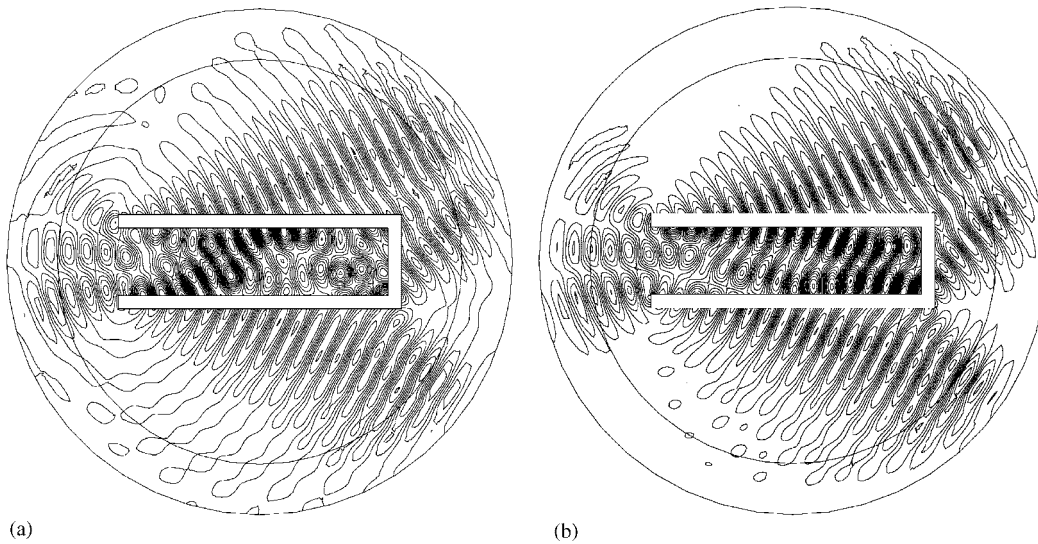


Figure 11. Scattering of a TE wave by a semi-open cavity: contours of: (a) $\text{Re}(H_z^s)$; and (b) $\text{Im}(H_z^s)$

4.2.2. NACA0012 aerofoil. The final example involves the simulation of the scattering of a TE wave by a perfectly conducting NACA0012 aerofoil. The chord length, c , of the aerofoil is assumed to be given by $c = 2\lambda = 1$. An unstructured mesh consisting of 499 triangles is used to discretize the region bounded internally by the aerofoil and externally by the circle of radius $r = 1.25$. The remaining area is bounded externally by the circle of radius $r = 2$ and is discretized with a structured mesh of 52 quadrilaterals. This mesh is shown in Figure 13 and

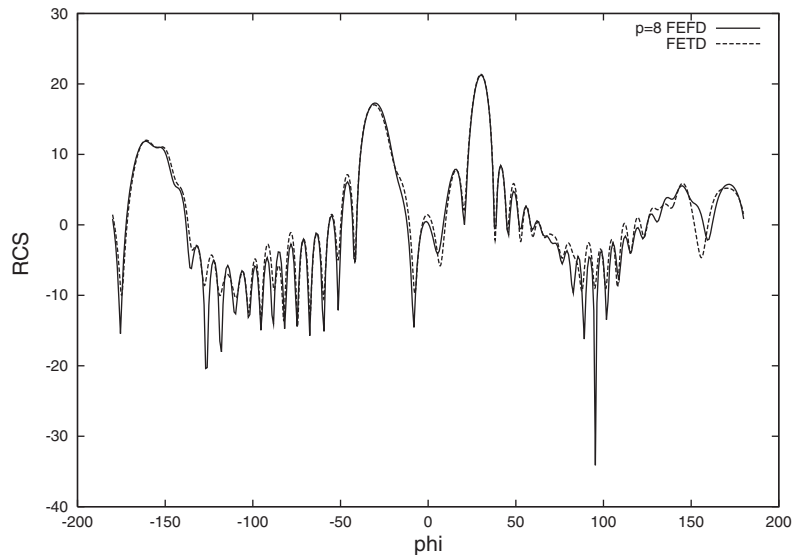


Figure 12. Scattering of a TE wave by a semi-open cavity: comparison of the computed RCS distribution with that produced by a time-domain finite element method.

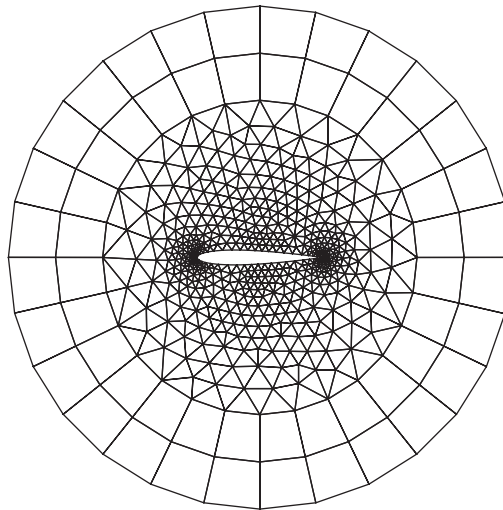


Figure 13. A hybrid mesh for the NACA0012 aerofoil consisting of 499 triangles and 52 quadrilaterals.

it can be seen that the mesh is refined near the leading and trailing edges of the aerofoil in order to provide the required geometrical definition. The PML layer for this example occupies the final layer of quadrilaterals in the structured mesh.

Two separate simulations are performed. The first involves illumination from the front of the aerofoil, while the illumination in the second simulation is from the rear. In each case, as before, the order of approximation employed is increased uniformly across the mesh until

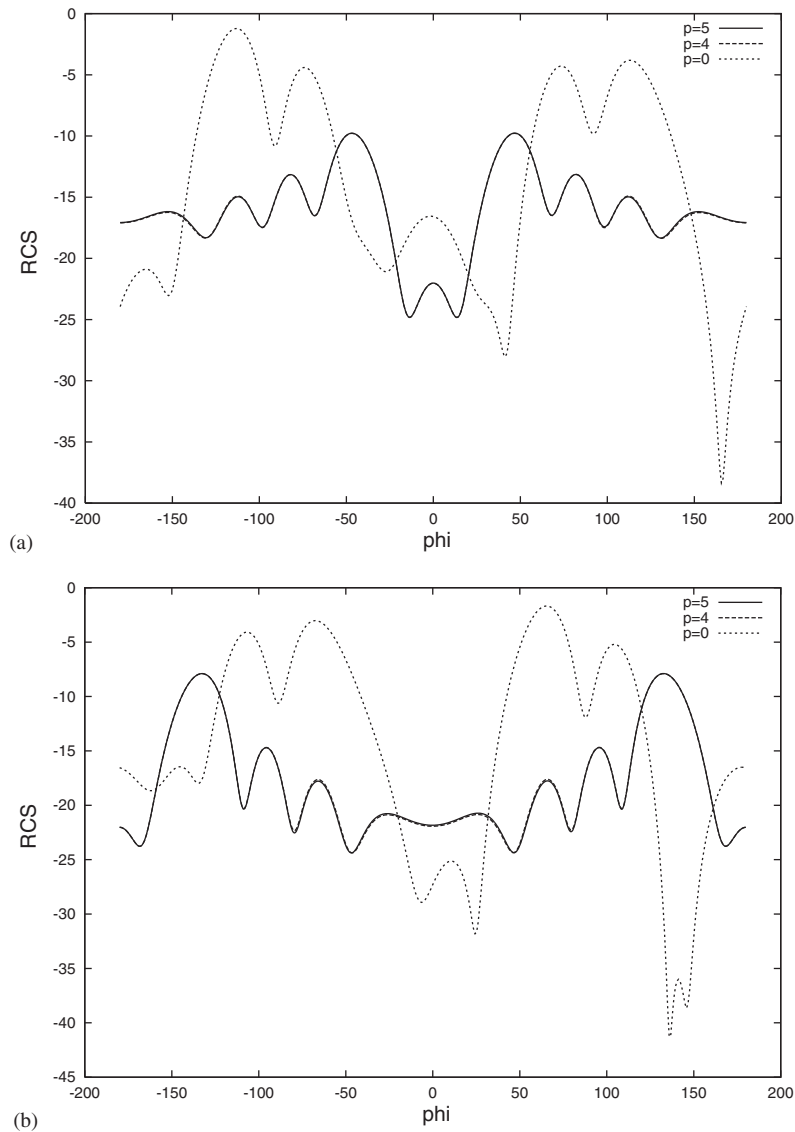


Figure 14. Scattering of a TE wave by a perfectly conducting NACA0012 aerofoil: computed RCS distributions when the aerofoil is illuminated: (a) from the front; and (b) from the rear.

convergence of the RCS distribution is obtained. The manner in which the mesh convergence is achieved is apparent from Figure 14 (a) and 14(b), which show the calculated RCS distributions. The initial solution, computed with order $p=0$ on each element, is asymmetric, reflecting the asymmetric nature of the mesh. However, with increase in the order p of the approximation employed, it is clear that the effect of the mesh becomes less important and the solution rapidly converges to a symmetric distribution.

5. CONCLUSION

We have described an arbitrary order hybrid edge element approach for the solution of electromagnetic scattering problems. The implementation of a non-reflecting condition at the truncated far-field boundary has been accomplished by the addition of a perfectly matched layer (PML). Simulations involving a cylindrical scatterer showed the advantages of the PML approach compared with the use of a second-order absorbing boundary condition. The method was then used to successfully simulate a number of more challenging problems. Future work will address the problem of error estimation, with the objective of providing a rigorous adaptive procedure incorporating an automatic h and p refinement capability. A three-dimensional extension of this work is also contemplated but this will only be successful for practical problems if an efficient iterative solver can be developed.

ACKNOWLEDGEMENTS

Paul Ledger acknowledge the support provided by the U.K. Engineering and Physical Sciences Research Council, in the form of a Ph.D. Studentship awarded under research grant GR/M59112. The authors acknowledge the insight provided by discussions with Professor Mark Ainsworth and Dr Joe Coyle, Department of Mathematics, Strathclyde University, and Dr David Rowse, BAE SYSTEMS Ltd, Advanced Technology Centres—Sowerby.

REFERENCES

1. Darve E, Löhner R. Advanced structured–unstructured solver for electromagnetic scattering from multimaterial objects. *AIAA Paper* 97-0863, 1997.
2. Morgan K, Brookes PJ, Hassan O, Weatherill NP. Parallel processing for the simulation of problems involving scattering of electromagnetic waves. *Computer Methods in Applied Mechanics and Engineering* 1998; **152**: 157–174.
3. Morgan K, Peraire J, Peiró J. Unstructured grid methods for compressible flows. *Report No: 787—Special Course on Unstructured Grid Methods for Advection Dominated Flows*, AGARD, Paris, 5.1–5.39, 1992.
4. Kamon M, Tsuk MJ, White JK. FASTHENRY: a multipole accelerated 3D inductance extraction program. *IEEE Transactions on Microwave Theory and Techniques* 1994; **42**:1750–1758.
5. Nédélec JC. Computation of eddy currents on a surface in \mathbb{R}^3 by finite element methods. *SIAM Journal of Numerical Analysis* 1978; **15**:580–594.
6. Nédélec JC. Mixed finite elements in \mathbb{R}^3 . *Numerische Mathematik* 1980; **35**:315–341.
7. Nédélec JC. A new family of mixed finite elements in \mathbb{R}^3 . *Numerische Mathematik* 1986; **50**:57–81.
8. Monk P. An analysis of Nédélec's method for the spatial discretization of Maxwells equations. *Journal of Computational and Applied Mathematics* 1993; **47**:101–121.
9. Monk P. On the p - and hp -extension of Nédélec's curl conforming elements. *Journal of Computational and Applied Mathematics* 1994; **53**:117–137.
10. Demkowicz L, Rachowicz W. A 2D hp -adaptive finite element package for electromagnetics (2Dhp90em). *TICAM Report* 98-15, University of Texas at Austin, 1998.
11. Demkowicz L, Vardapetyan L. Modeling of electromagnetic/scattering problems using hp -adaptive finite elements. *Computer Methods in Applied Mechanics and Engineering* 1998; **152**:103–124.
12. Ainsworth M, Coyle J. Hierarchic hp -edge element families for Maxwell's equations on hybrid quadrilateral/triangular meshes. *Computer Methods in Applied Mechanics and Engineering* 2001; **19**:6709–6733.
13. Cecot W, Demkowicz L, Rachowicz W. A two dimensional infinite element for Maxwell's equations. *Computer Methods in Applied Mechanics and Engineering* 2000; **188**:625–643.
14. Berenger J-P. A perfectly matched layer for the absorption of electromagnetic waves. *Journal of Computational Physics* 1994; **114**:185–200.
15. Kuzuoglu M, Mittra R. Investigation of nonplanar perfectly matched absorber for finite element mesh truncation. *IEEE Transactions on Antennas and Propagation* 1997; **45**:474–486.
16. Courant R, Hilbert D. *Methods of Mathematical Physics*, vol. 2. Wiley: New York, 1962.
17. Bayliss A, Turkel E. Radiation boundary conditions for wave-like equations. *Communications in Pure and Applied Mathematics* 1980; **33**:707–725.

18. Peterson AF. Absorbing boundary conditions for the vector wave equation. *Microwave and Optical Technical Letters* 1988; **1**:62–64.
19. Givoli D. *Numerical Methods for Problems in Infinite Domains*. Elsevier: Amsterdam, 1992.
20. Bettess P. *Infinite Elements*. Penshaw Press: Sunderland, 1992.
21. Astley RJ. Mapped spheroidal wave-envelope elements for unbounded wave problems. *International Journal for Numerical Methods in Engineering* 1988; **41**:1235–1254.
22. Jin J-M, Volakis JL, Collins JD. A finite element-boundary integral method for scattering and radiation by two- and three-dimensional structures. *IEEE Antennas and Propagation Magazine* 1991; **33**:22–32.
23. Salazar-Palma M, Sarker TK, García-Castillo L-E, Djordjević A. *Iterative and Self Adaptive Finite Elements in Electromagnetic Modeling*. Artech House: London, 1998.
24. Ledger PD. Edge elements for waveguide and scattering problems. *Masters Thesis*, University of Wales, Swansea, 1999.
25. Webb JP, Forghani B. Hierarchical scalar and vector tetrahedra. *IEEE Transactions on Magnetics* 1993; **29**: 1495–1498.
26. Miniowitz R, Webb JP. Covariant projection quadrilateral elements for the analysis of waveguides with sharp edges. *IEEE Transactions on Microwave Theory and Techniques* 1992; **39**:501–505.
27. Abramowitz M, Stegun IA. *Handbook of Mathematical Functions with Formulas, Graphs and Mathematical Tables*. National Bureau of Standards: Washington DC, 1964.
28. Stratton JA. *Electromagnetic Theory*. McGraw-Hill: New York, 1941.
29. Ledger PD, Morgan K, Hassan O, Weatherill NP. A hybrid arbitrary order edge element scheme for electromagnetic scattering. *Proceedings of the ECCOMAS CFD2001 Conference*, Swansea, 2001.
30. Kardestuncer H. *Finite Element Handbook*. McGraw-Hill: New York, 1987.
31. Liu W, Sherman AH. Comparative analysis of the Cuthill–McKee and the reverse Cuthill–McKee ordering algorithms for sparse matrices. *SIAM Journal of Numerical Analysis* 1976; **13**:198–213.
32. Taflov A, Hagness SC. *Computational Electrodynamics: The Finite Difference Time Domain* (2nd edn). Artech House: Boston, London, 2000.
33. Balanis CA. *Advanced Engineering Electromagnetics*. Wiley: New York, 1989.
34. Yao-Bi JL, Nicolas L, Nicolas A. Modeling unbounded wave propagation problems in terms of transverse fields using 2D mixed elements. *IEEE Transactions on Magnetics* 1995; **31**:1594–1597.
35. Hassan O, Morgan K, Weatherill NP. The effect of inaccuracies in geometry modelling on the results of electromagnetic scattering simulations. *Communications in Numerical Methods in Engineering*, 2002, submitted.
36. Peraire J, Vahdati M, Morgan K, Zienkiewicz OC. Adaptive remeshing for compressible flow computations. *Journal of Computational Physics* 1987; **72**:449–466.
37. Morgan K, Hassan O, Peraire J. A time-domain unstructured grid approach to the simulation of electromagnetic scattering in piecewise homogeneous media. *Computer Methods in Applied Mechanics and Engineering* 1996; **134**:17–36.